MDPI

Article

An Optimized Additive Manufacturing Strategy for Low-Impedance Electronics

Tobias Hehn [1,2,*], Felix Zimmer [2], Markus Klein [1,*] and Jens Holtmannspötter [1,2]

[1] Department of Aerospace Engineering, University of the Bundeswehr Munich, 85579 Neubiberg, Germany
[2] Bundeswehr Research Institute for Materials, Fuels and Lubricants 2, 85435 Erding, Germany
* Correspondence: tobiashehn@bundeswehr.org (T.H.); markus.klein@unibw.de (M.K.)

Abstract: The additive manufacturing of electronics allows the printing of complex structures, such as antenna matrixes, motors, and system-in-packages, directly into a three-dimensional shape. This freedom enables new design approaches for various applications in different fields. The additive manufacturing system under investigation uses inkjet technology, which is capable of applying a conductive and a non-conductive ink layer-by-layer at the desired places. This layer-by-layer approach creates a rough outline of the conductive material that negatively impacts high-frequency signal transmission. This article proposes a blockwise printing strategy to smooth the contours of the conductive material, enhancing its high-frequency properties. The evaluation of representative geometries, resembling printed samples that can be obtained using a custom slicing software, showed that the blockwise strategy reduced electrical losses by a factor of two compared to the conventional layer-by-layer approach. Numerical simulations demonstrated that this method achieves improved impedance performance in materials with low-loss tangents. These findings highlight the potential of alternative additive manufacturing strategies to optimize high-frequency performance in electronic devices.

Keywords: additive manufacturing of electronics; inkjet technology; material jetting; AM strategy; high-frequency properties

Academic Editor: Andrea Bonci

Received: 13 January 2025
Revised: 5 February 2025
Accepted: 7 February 2025
Published: 11 February 2025

Citation: Hehn, T.; Zimmer, F.; Klein, M.; Holtmannspötter, J. An Optimized Additive Manufacturing Strategy for Low-Impedance Electronics. *Electronics* **2025**, *14*, 695. https://doi.org/10.3390/electronics14040695

Copyright: © 2025 by the authors. Licensee MDPI, Basel, Switzerland. This article is an open access article distributed under the terms and conditions of the Creative Commons Attribution (CC BY) license (https://creativecommons.org/licenses/by/4.0/).

1. Introduction

Additive manufacturing of electronics (AME) is being developed as a promising application in additive manufacturing (AM). AME allows a new design approach, a significant improvement in performance, and a reduction in environmental impact [1]. With AME, traces can not only be routed freely on a circuit board [2] but also in various other geometric shapes [3,4]. This flexibility enables the integration of components such as capacitors, coils, heatsinks, and shielding directly into a three-dimensional structure, moving the boundaries of electromechanical integration [5,6]. In addition, more complex structures such as antenna matrixes [7–10], motors, sensors [11], filters [4], and system-in-packages [12,13] are printable, leading to highly customizable electronics [14]. This multifunctional capability of additive manufacturing has been explored to integrate mechanical, electrical, and optical functionalities, further broadening its application scope in creating advanced sensors and devices. The approach also enables the integration of structural elements, such as the casing, directly with the electronic circuitry, eliminating the need for separate housings or mounting boards. This enhances design freedom, packaging density, and electromechanical integration [15–19].

The printing process used in this work employs inkjet technology to apply non-conductive and conductive material. Inkjet printing is an AM process that enables the

creation of three-dimensional (3D) objects by depositioning multiple materials at the same stage of the object's manufacture. The process uses two print heads, each containing a multitude of nozzles, which eject droplets of ink onto a build platform. By moving the print head relative to the substrate in the xy-plane, a layer of material is processed [20–24]. After the deposition of each layer, a curing mechanism is applied to solidify the current layer to a rigid structure. By consecutively stacking layers on top of each other, the process gradually forms a 3D object. Inkjet's ability to utilize multiple materials in a single build enables the creation of objects with varying properties, such as different colors, transparencies, and mechanical or electrical properties [5,19,21,23,25].

By using a conductive and a non-conductive ink, these varying properties can be electrically conductive wires in an insulating housing [26]. By using these two inks in a multi-material AM process, printed conductive traces can be built in an insulating body. As this process applies both inks layer-by-layer, the resulting shape at the outline of the conductive material is mainly influenced by the wetting effect of the ink on the substrate. This phenomenon has been studied extensively, revealing the role of material compatibility and precision in achieving smooth, defect-free conductive paths, which are critical for improving performance [27,28]. Due to the high similarity of the cured substrate to the liquid ink, a good wetting behavior typically occurs, resulting in broad and flat droplets before the curing process [29]. Solidifying these shapes and stacking them on top of one another leads to a rough outline of the electrically conductive traces, as shown in Figure 1. Therefore, the layer-by-layer approach of this method introduces a surface roughness at material interfaces, which can negatively impact high-frequency signal transmission. This is primarily due to the skin-effect, where the alternating current concentrates at the conductor's surface, amplifying the influence of surface irregularities on the impedance [30–32]. Earlier research has highlighted the fact that the interface quality in high-frequency applications is a critical factor in minimizing these effects, emphasizing the need for strategies that enhance smoothness at the material boundaries [33]. The main idea of this paper is to use a different AM strategy to smooth the outline of the solidified conductive material to reduce the losses caused by the skin-effect.

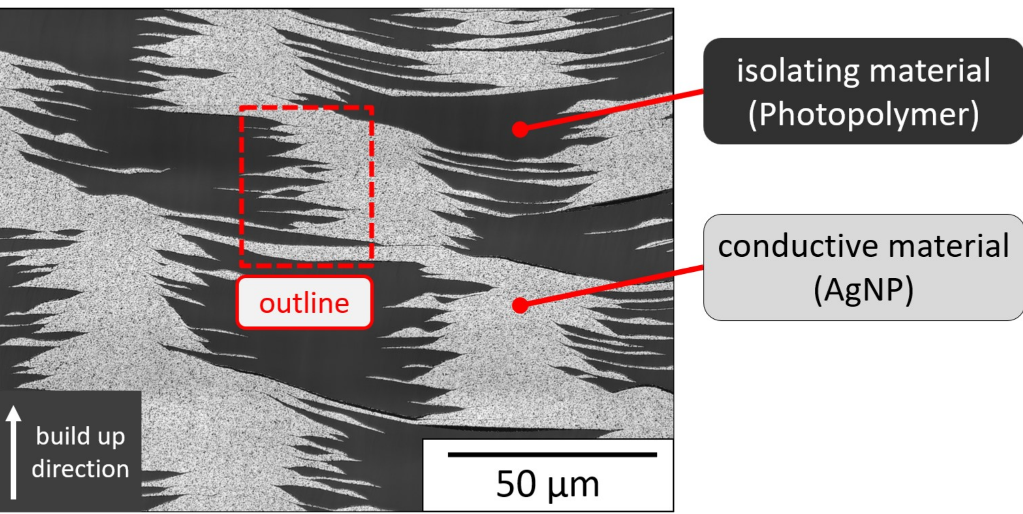

Figure 1. Cross-sectional image of an additively manufactured test specimen. The bright areas are electrically conductive structures made of sintered silver nanoparticles. The dark areas are the insulating photopolymer. The area marked in red shows the outline of the conductive material. The cross-section surface was milled using an argon ion beam.

The proposed strategy was evaluated using representative 3D geometries derived from printed samples and analyzed through numerical simulations. The results indicate

that the blockwise strategy reduces electrical losses by a factor of two compared to conventional approaches, particularly for low-loss tangent materials. These findings demonstrate the potential for significant improvements in the design and performance of additively manufactured electronics, enabling new applications in high-frequency systems.

2. Methods and Modelling

This section first focuses on how the commonly applied AM strategy influences the microstructure of the printed outline and how the proposed strategy is expected to impact this microstructure. A comparative analysis between the layer-by-layer and the blockwise AM strategy is presented using cross-sectional images of printed samples. Subsequently, the process of defining replacement geometries for the simulation is shown. Afterwards, the setup of both numerical simulations, including material properties, boundary conditions, and mesh parameters, is described.

The experiments were conducted using a Nano Dimension DragonFly IV inkjet printer, a specialized additive manufacturing system for electronics, manufactured by Nano Dimension Ltd., Ness Ziona, Israel [26,34]. This printer employs two print heads, one for a conductive silver nanoparticle (AgNP) ink and another one for an ultraviolet (UV) curable dielectric polymer ink [35,36]. The conductive ink consists of silver nanoparticles with an average diameter of 70 nm at a content of 50 wt%, provided by Nano Dimension, while the UV-curable dielectric photopolymer ink is a proprietary formulation optimized for electrical insulation [37].

To implement the proposed blockwise printing strategy, a custom slicer developed by the authors was used. This software allows precise control of the sequence of layers, enabling the deposition of multiple layers of one material before switching to the other. The slicing software outputs image stacks and corresponding text files containing layer height information, which are compatible with the DragonFly IV system. The custom slicer was tested with a proof-of-concept design, and its effectiveness was evaluated through numerical simulations and cross-sectional imaging of printed samples.

2.1. Influence of the AM Strategy

The current AM strategies are based on applying the individual layers one after the other. In the inkjet machine used, this is implemented by first applying conductive ink at the conductive areas of one layer. After that, the solvent of the conductive ink is evaporated and the AgNPs are sintered using infrared light. In the second step, the non-conductive ink of this layer is processed and cured using ultraviolet light. After completing one layer consisting of conductive and non-conductive areas, the process is repeated [26,34–37].

While the current AM strategy follows a layer-by-layer approach, the proposed strategy uses a blockwise printing approach. This method intentionally prints multiple consecutive layers of one material before switching to the other, specifically to optimize the interface geometry and reduce roughness, exceeding the capabilities of the conventional layer-by-layer process. The concept is based on the idea that the interface can be significantly smoothed if the droplets of different inks cannot lie on top of each other in the single droplet scale. This can be achieved by printing the dielectric material for multiple layers, then switching to the conductive material, and printing the conductive material for the same number of layers. As the droplets do not have their neighbor-droplet in each layer, this is expected to result in an improved interface geometry and, therefore, better HF properties. Although the proposed blockwise AM strategy significantly reduces surface roughness by minimizing the number of spikes per length unit, residual geometrical imperfections remain due to persistent wetting effects—but at a larger scale. A schematic comparison of the current and suggested strategy is shown in Figure 2.

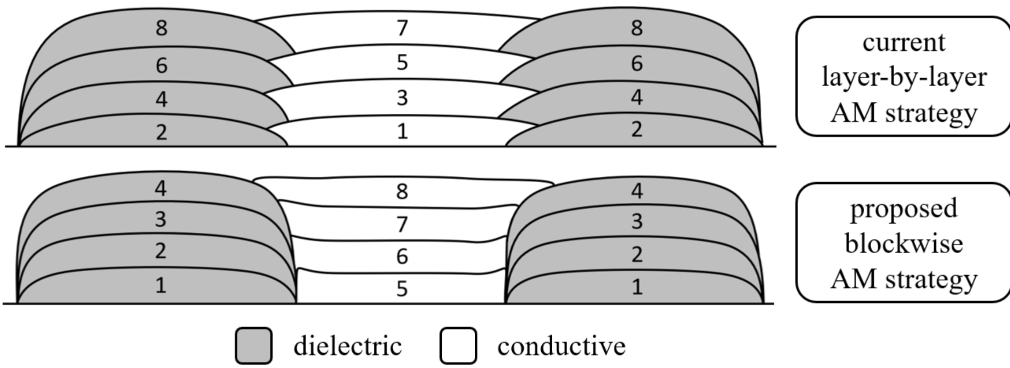

Figure 2. Schematic comparison of the current layer-by-layer approach (**top**) and the proposed blockwise AM strategy (**bottom**). The numbers indicate the sequence of droplet application. Grey droplets represent the dielectric material, while white shapes represent the conductive material. The blockwise approach aims to minimize surface roughness along the build-up direction, indicated from **bottom** to **top**.

The motivation for the proposed blockwise printing approach is to minimize the negative effects caused by the skin-effect in electrical conductors [30–32]. The skin-effect cannot be entirely eliminated, but the influence on the impedance can be reduced by smoothing the outline. In a circular conductor, the penetration depth, δ, of electrical current decreases with higher frequency, permeability, and conductivity. Due to asymptotic behavior as shown in Figure 3, the penetration depth is given at the point where the current density, J, decays to $1/e$ of the surface current density, J_0, approximately 37%, resulting in $J = J_0 \cdot e^{-1} \approx 0.37 J_0$ (A/m²).

$$\delta = \sqrt{\left(\frac{2}{\omega \mu \sigma}\right)} \qquad (1)$$

where:

ω = angular frequency
μ = magnetic permeability
σ = electrical conductivity

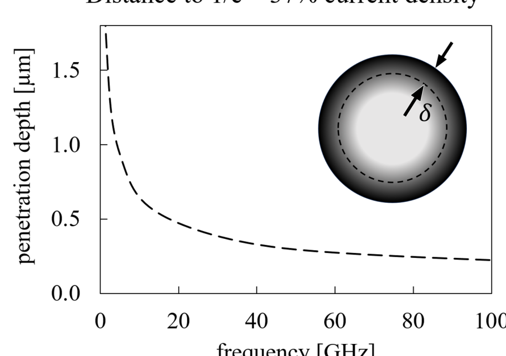

Figure 3. Penetration depth at a perfect circular conductor. **Left**: Penetration depth, δ, as a function of frequency and material properties [30–32]. **Right**: Penetration over excitation frequency using the material properties of bulk silver. The circle is a schematic illustration of the penetration depth at $J = J_0 \cdot e^{-1} \approx 0.37 J_0$ (A/m²).

This equation shows that higher frequencies (ω), increased permeability (μ), or enhanced conductivity (σ) reduce the penetration depth, concentrating the current closer to the conductor's surface. Smoothing the outline reduces the associated impedance losses by ensuring a more uniform current distribution at these reduced penetration depths.

2.2. Geometries for the HF-Simulation

The proposed AM strategy was tested using a custom slicer for the Nano Dimension DragonFly IV machine. Afterwards, the samples were examined in cross-section. This procedure was also carried out using the standard layer-by-layer process. From these investigations, representative geometries were derived and subsequently analyzed using numerical simulation.

To obtain the desired behavior, the custom slicer starts printing at a start level and prints a defined number of layers of the dielectric material from there. After completing, the slicer returns to the base level of the block and prints the same number of layers using the conductive material. This process is repeated until the part is finished. Figure 4 shows specimen cross-sections produced using each printing strategy. Since both images were taken at the same magnification, the influence of the printing strategy can be shown in a direct comparison based on the waviness of the boundary between the conductive material and dielectric material. In this example, the block height was set to four layers, which results in a block height of $h = 4 \cdot 11$ µm, as also presented in Figure 5. The geometric shape of conductive and isolating material does not change from one block to the next. The number of layers could be increased, which should even enlarge the smoothness of the outline.

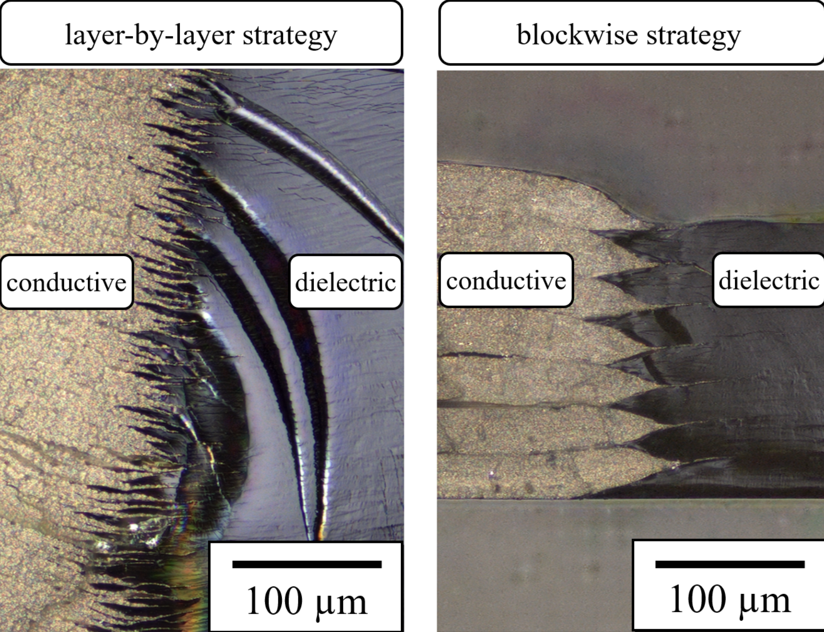

Figure 4. Cross-sectional images of printed samples using the current layer-by-layer strategy (**left**) and the proposed blockwise strategy (**right**). The bright area represents conductive material and the darker area is the dielectric material. Images were obtained with a custom slicer on the Nano Dimension DragonFly IV machine.

Both images of Figure 4 show that the length of the overlapping area is nearly unaffected. The parameter that changes is the waviness of the roughness in the vertical z-direction. These shapes were transformed into representative geometries through the stacking of conic sections in the build-up direction, as shown in Figure 5. The geometry is characterized by the identical "waviness amplitude" in both compared outlines. Together with the ideal reference geometry, three geometries were numerically investigated:

1. A geometry based on the current layer-by-layer printing strategy.
2. A geometry based on the proposed blockwise strategy.
3. An ideal geometry to reference the behavior with an ideal smooth outline.

As shown in Figure 5, the geometrical parameter that changes between the current and proposed AM strategy is the height of the individual elements, which corresponds to the height of the printed blocks. As a result, the average diameter, r_n, of both the trace and the shielding remains identical. This average diameter is also the diameter of the compared ideal structure.

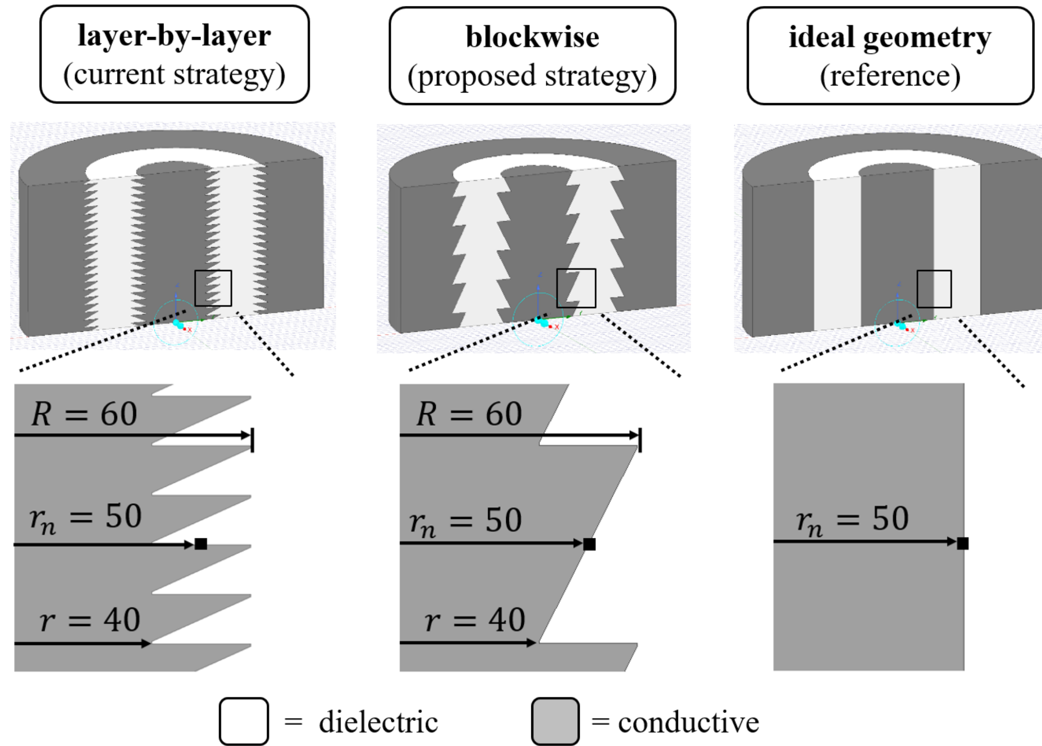

Figure 5. Abstraction of the printed structures to representative 3D geometries. **Left**: 3D geometry of the current AM strategy; middle: blockwise AM strategy; **right**: ideal shape for comparison purposes. The numbers indicate the characteristic radii of the inner conductor. The black squares indicate the center of the respective line. All values are in µm.

The nominal diameter of the inner conductor is set to 100 µm, representing the medium diameter of the simulated geometries. The size of the outer conductor is based on the necessary dimensions of a coaxial line with a wave impedance of $Z_0 = 50\,\Omega$ [30,38] according to

$$Z_0 = \frac{1}{2\pi}\sqrt{\frac{\mu}{\epsilon}}\ln\left(\frac{D}{d}\right) \tag{2}$$

where:

d = outer diameter of the inner line
D = inner diameter of the outer line
ϵ_r = relative permittivity of the insulating material
μ_r = relative permeability of the insulating material

These three geometries were each simulated using three material combinations. The material of both inner and outer conductors in each simulation is 'silver' from the Ansys materials database. The insulator material is chosen to be either 'Zeonex RS420 (ZEO)', 'Polyethylene (PE)', or 'FR4' since these materials cover a wide range of dissipation factor $\tan(\delta)$ from 0.0002 to 0.02. A high loss tangent indicates that a large amount of energy is lost in heat, while a low loss tangent indicates that losses are small [39–42].

Since the thickness of the insulating layer between the inner conductor and the outer conductor depends on the relative permittivity, ϵ_r, of the insulating material, the geometries were adapted to the dielectric material used in the simulations to match the goal of $Z_0 = 50\,\Omega$. Table 1 shows the electrical and geometrical properties used in the simulations.

Table 1. Material properties and geometric values of the simulation setup. The material properties are extracted from the Ansys materials database. The geometric values are based on the target impedance of $Z_0 = 50\,\Omega$.

	Relative Permittivity ε_r [-]	Relative Permeability μ_r [-]	Bulk Conductivity σ [S/m]	Dissipation Factor $\tan\delta$ [-]	Diameter Inner/Outer d/D [µm]
Silver	1.00	0.99998	61×10^6	0	100.0 (outer)
FR4 epoxy	4.40	1	0	0.02	576.0 (inner)
Polyethylene	2.25	1	0	0.001	349.4 (inner)
Zeonex RS420	2.30	1	0	0.0002	354.0 (inner)

The height of one printing block, which means the number of layers of each block, can be adjusted and even extended beyond the inscribed number of four until the distance between the printhead and substrate is fully utilized—assuming that the geometry to be printed remains the same from block to block. To avoid sub-droplet roughness caused by the coffee-stain effect, where particles accumulate at the edges during solvent evaporation [43–45], the photopolymer is printed first. As this AM strategy focuses on freely routed 3D shapes, the simulation setups represent coaxial lines oriented orthogonal to the build-up direction, i.e., from bottom to top or from top to bottom. The length of the simulated geometry is set to 200 µm. In order to convert the results into the scale-independent unit of 1/mm, the results are corrected accordingly.

2.3. Numerical Simulation of the HF-Properties

The suggested strategy is evaluated by numerical simulations using the Ansys High-Frequency Structure Simulator (HFSS) and the Ansys Quasi-Static 3D Electromagnetic Field Solver (Q3D), both developed by Ansys Inc., headquartered in Canonsburg, Pennsylvania, USA. They use the finite element method (FEM) to solve Maxwell's time-harmonic equations iteratively [46,47]. Both solvers are able to quantify the behavior of electrical structures, where Ansys HFSS is used to quantify the overall power loss and Ansys Q3D is used to trace back to an analytical equivalent circuit for HF lines.

The S21 parameter is used to express the power loss of each geometry and material combination. It indicates the power loss from measuring point to measuring point in decibels (dB), considering losses due to electrical resistance, inductance, capacitance, and conductance (RLCG). In the second step, each of these RLCG parameters is analyzed using the Q3D solver to determine the cause of the losses. With these values, the equivalent circuit of a coaxial line can be characterized with frequency-dependent characteristic values. The following section briefly outlines the four Maxwell equations used in the simulations and gives an overview of the comprehensive equation, which is solved iteratively.

Gauss's law for the electric field describes how electric charges generate electric fields. The line integral of the electric field around any closed surface is proportional to the total charge enclosed within the surface [48–50]:

$$\nabla \cdot E = \frac{\rho}{\epsilon_0} \tag{3}$$

where E is the electric field, ρ is the charge density, and ϵ_0 is the electric constant (vacuum permittivity). ∇ is the curl operator in the following equations. Second, Gauss's law for the magnetic field states that there are no magnetic monopoles and that magnetic field lines always form closed loops [48–50]:

$$\nabla \cdot B = 0 \tag{4}$$

where B is the magnetic field. Faraday's law of induction describes how changing magnetic fields generate electric fields. Third, the induced electric field is proportional to the rate of change of the magnetic field [48–50]:

$$\nabla \times E = -\frac{\partial B}{\partial t} \quad (5)$$

where E is the electric field and B is the magnetic field. Fourth, Ampere's circuital law relates the circulation of the magnetic field around a closed loop to the electric current passing through the loop. It also includes a term for the displacement current arising from a changing electric field [48–50]:

$$\nabla \times B = \mu_0 (J + \epsilon_0 \frac{\partial E}{\partial t}) \quad (6)$$

where B is the magnetic field, J is the current density, μ_0 is the magnetic constant (vacuum permeability), and ϵ_0 is the electric constant. According to the documentation of the Ansys Electronics suite [51,52], both HFSS and Q3D solve the following equation iteratively based on the previously presented Maxwell equations:

$$\nabla \times \left(\frac{1}{\mu_r} \nabla \times E_m(x,y) e^{-\gamma_m z} \right) - k_0^2 \epsilon_r E_m(x,y) e^{-\gamma_m z} = 0 \quad (7)$$

where:

$\nabla \times$ = Curl operator, describing the rotational field of a vector field
$\mu_r(x,y)$ = Complex relative permeability
∇ = Nabla operator, representing spatial derivatives
$E_m(x,y)$= Electric field mode pattern of mode m
$\gamma_m = \alpha_m + j\beta_m$
α_m = Attenuation constant of mode m
β_m= Propagation constant of mode m
k_0= Wave number of free space
$\epsilon_r(x,y)$= Complex relative permittivity

2.4. Setup of the Simulation Boundary Conditions

The numerical simulation of the HF parameters was carried out using the Ansys Electronics Suite 2022 software package and the HFSS and Q3D solvers contained therein. The software is developed by Ansys Inc., headquartered in Canonsburg, Pennsylvania, USA The simulations aim to obtain a quantitative estimate of the influence of the printing strategy. The previous printing strategy, the proposed blockwise printing strategy, and a reference are compared.

In HFSS, a wave port was defined at each end of the coaxial line. This wave port covers the entire coupling area, including the inner, outer, and insulating areas. The simulation software automatically creates the flat cylinders shown in green in Figure 6 to match the wave impedance. They are made of 'pec' (perfect electrical conductor) material.

The edges of the abstracted geometries are flattened with a 1 µm vertical line to prevent geometrically sharp edges. The top and bottom units of the repeating structures are half-elements to ensure the same surface at the contact face of the wave port for a symmetrical simulation setup along the measurement line. A convergence study performed on mesh refinement has shown that using a mesh that enters each branch of the roughness with a sufficient number of elements is essential. Using a mesh that is too coarse ignores the outline of the structure and leads to incorrect simulation results. Therefore, the mesh refinement is set to a maximum length of 6 µm as this means that the mesh must form at

least three nodes in each branch to represent the topology of the outline correctly. This provides a sufficient starting point for the dynamic mesh refinement, set to the finest level provided by Ansys (level 9).

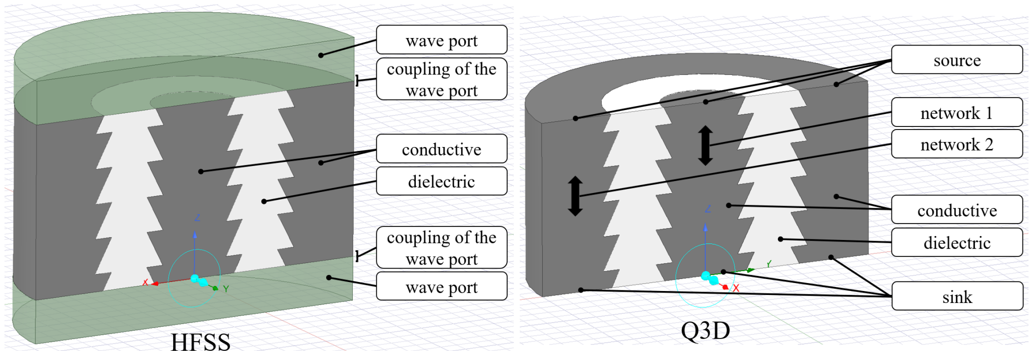

Figure 6. Setup of the HFSS simulation (**left**) and Q3D simulation (**right**) as cross-sections of the simulated geometries. A special feature of the design is the half-repeating unit at each wave port, resulting in a balanced impedance at both ends of the coax line. The green parts at the bottom and top of the HFSS simulation are the wave ports out of a perfect electrical conductor assigned by Ansys. The setup of the Q3D simulation consists of a separate network for the inner conductor as well as for the outer conductor. The excitation is performed via a pair of sink and source for each of these networks.

The frequency range of the sweep varies from 0.1 GHz to 100 GHz. Since the simulation software controls the mesh refinement based on the base frequency, the base frequency was set to the maximum frequency of 100 GHz. This ensures the HF parameters are determined over the entire frequency range, with the same sufficiently fine mesh for all frequencies.

For the Q3D simulation, the same geometries, materials, and frequency ranges were used for the HFSS simulation. The boundary conditions were selected to assign the inner and outer conductors to their specific network. Each of these networks was finally assigned a source and a sink at the end faces.

3. Results and Discussion

This section begins with the analysis of the overall damping of the simulated geometries using the S21 parameter diagrams. The S21 parameter, which represents the transmission coefficient, quantifies the ratio of the output power to the input power in a two-port network as a function of frequency. It indicates how much power is transmitted through the structure and how much of it is lost, making it critical for evaluating high-frequency performance. Subsequently, the results of the Q3D simulations are presented, enabling the extraction of total loss contributions and their allocation to the individual elements of an equivalent circuit model for a coaxial transmission line. These simulations allow for the frequency-dependent determination of equivalent circuit components, including inductance (L), resistance (R), conductance (G), and capacitance (C). This approach provides insights into the causes of the observed losses and their relation to the geometry and material properties of the printed structures.

3.1. Results of HFSS Simulation

Figure 7 shows three S21 diagrams, each containing the losses of one dielectric material in combination with all three representative geometries. A perfect lossless transmission would produce a horizontal line at 0 dB. Therefore, the deviations from 0 dB represent the power loss of geometry and material effects. Since the dielectric and conductive materials used in all simulations represented in the graphs are identical, it is assumed that the observed differences in damping are entirely due to geometric effects, which result from the different printing strategies. The simulation results in Figure 7 show a significant effect

of the surface shape on HF performance. Although the ideal shape is not lossless due to damping effects in the dielectric material, the damping losses change with the electrical frequency and interface shape.

It can be observed that dielectric losses increase with increased loss tangent, which is the expected behavior (for material properties, see Table 1). Using Zeonex or PE, where the loss tangents are $\tan(\delta_{ZEO}) = 0.0002$ and $\tan(\delta_{PE}) = 0.001$, respectively, the losses are mainly influenced by geometrical factors. Using a dielectric material with a higher loss tangent, it can be observed that the geometric influence is superimposed by the dielectric losses caused by the material itself.

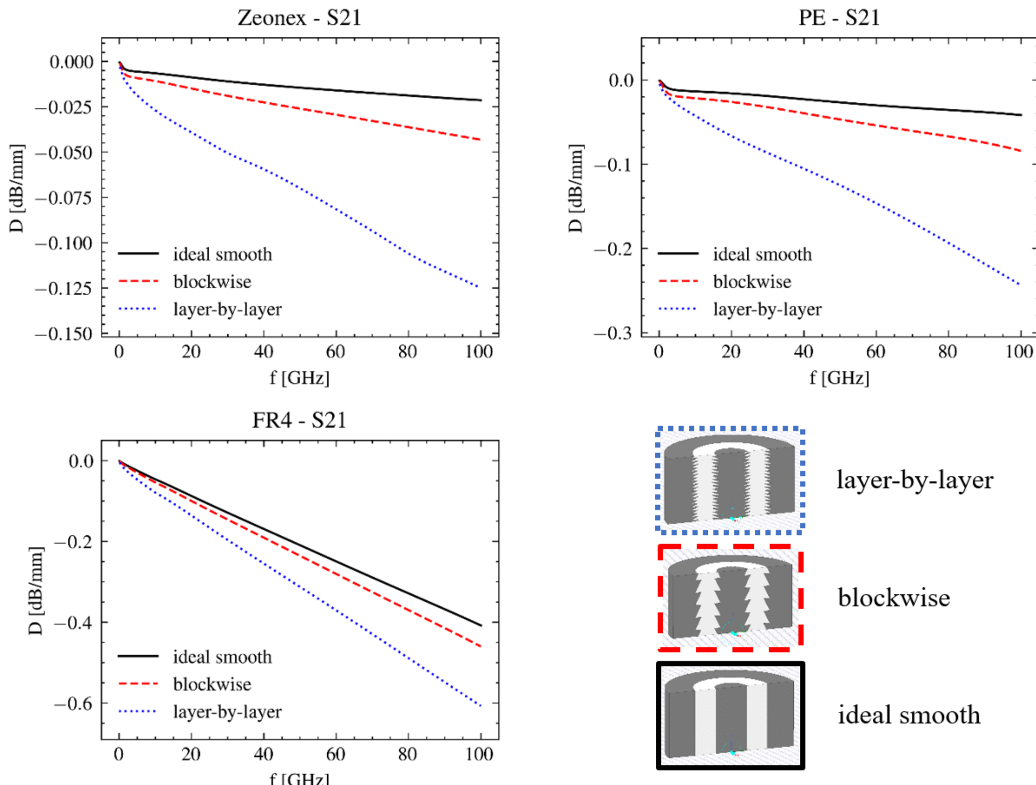

Figure 7. HFSS simulation results showing S21 parameter sweeps (0.1–100 GHz) for three geometries: ideal smooth, blockwise, and layer-by-layer. Results are presented for different dielectric materials: Zeonex, polyethylene (PE), and FR4. Schematic sketches of the geometries are provided in the lower right corner. The adaptive frequency sweep error tolerance was set to 0.2%, resulting in approximately 200 frequencies simulated per sweep.

3.2. Results of Q3D Simulation

An additional Q3D simulation with identical geometries was performed to identify the reason for the enlarged impedance. This simulation enables the breakdown of the impedance to the elements of an equivalent circuit diagram, as shown in Figure 8. Both the left and right ends of the traces represent a gate, which corresponds to the ends of a coaxial cable. The transmission line can be replaced by an inductance (L) and an ohmic resistance (R). The interaction of the inner and outer conductors represents a capacitance (C), which is not perfectly isolated and therefore has a conductance (G).

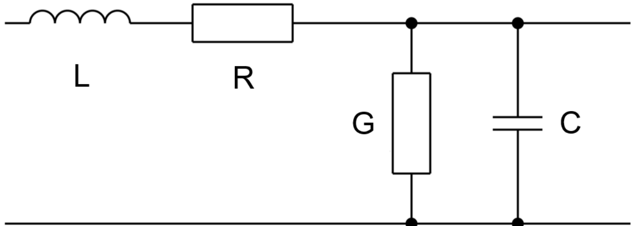

Figure 8. Equivalent circuit diagram of the simulated coax line containing the elements inductance (L), resistance (R), conductivity (G), and capacitance (C).

The result of the Q3D simulation is represented by four graphs using the dielectric material Zeonex as an example in Figure 9. The three lines per graph represent the 3D geometries and, therefore, the AM strategy. The influence of the geometry on the frequency-dependent values for inductance, capacitance, and conductance is less than 20%.

In contrast, the behavior of the ohmic resistance is dominant (>300%) and consistent with the idea that the current density at the surface increases with increased frequency. The higher current density leads to a decrease in the cross-sectional area through which the current flows, causing the ohmic resistance to increase. While experiments are not possible, the simulation results align with the expected behavior and known theoretical models that describe the impact of surface roughness on high-frequency performance. Specifically, the results are consistent with the principles outlined in widely accepted models, such as the Huray roughness model, which demonstrates how increased surface roughness leads to elevated current crowding and resistive losses at high frequencies [53].

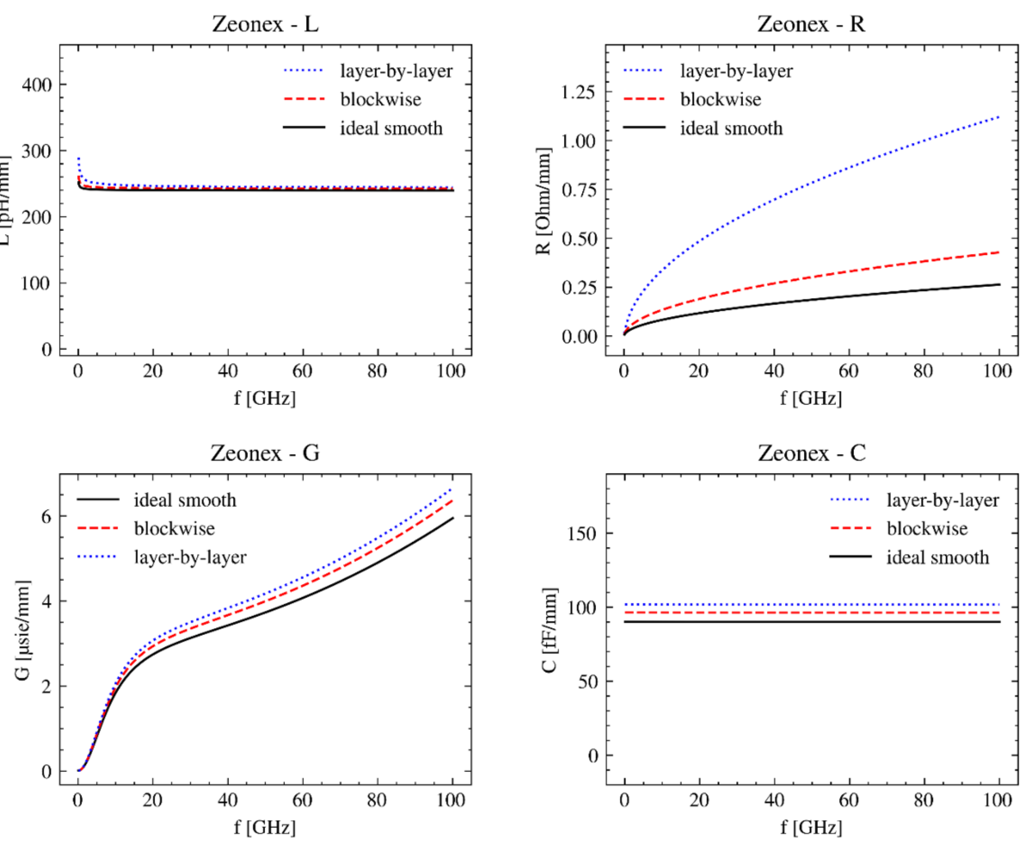

Figure 9. Results of the Q3D-Analysis. The plots show the behavior of inductance (L), resistivity (R), capacitance (C), and conductivity (G) at frequencies of 0.1 to 100 GHz for each representative geometry.

This agreement between the simulation and theoretical predictions reinforces the validity of the proposed blockwise printing strategy and shows its potential to mitigate roughness-related losses. Furthermore, the trends observed in the simulation data, such as the reduction of ohmic losses in smoother geometries, corroborate established literature on the relationship between surface roughness and impedance. While direct experimental validation of high-frequency properties was not feasible due to limitations in measurement equipment, the printed samples and their cross-sectional images provide valuable insights. These images demonstrate the smoother interface geometry achieved by the blockwise printing strategy compared to the layer-by-layer approach. This structural improvement aligns with theoretical expectations on reduced impedance losses at high frequencies.

4. Conclusions and Outlook

This study presents an optimized additive manufacturing strategy for creating low-impedance electronic structures using a blockwise 3D printing approach. The proposed method improves the interface geometry between conductive and dielectric materials, resulting in smoother outlines that mitigate roughness-related losses. Numerical simulations demonstrate that the blockwise strategy reduces electrical losses by up to 50% compared to the conventional layer-by-layer approach, particularly for low-loss tangent materials. While experimental validation of high-frequency properties was not feasible due to hardware limitations, cross-sectional images of printed samples confirm the structural improvements that lead to lower HF losses predicted by simulations.

The findings highlight the potential of the blockwise printing strategy to enhance high-frequency performance in additively manufactured electronics, paving the way for more efficient and reliable designs in applications such as antennas, sensors, and high-speed interconnects. Future research could explore experimental validation of high-frequency performance, the development of advanced materials with optimized properties, and the application of this strategy to more complex geometries and use cases.

Future investigations could further smooth the interface between the conductive and non-conductive material by using materials with optimized properties and by considering new AM strategies. In addition, using an AM machine with a resolution smaller than the droplet diameter might be promising—this way, the droplets do not have to be placed directly on top of each other and could create an even steeper outline through a slight offset in the droplet stacking. The presented work intends to show the potential of alternative AM strategies in the field of additively manufactured electronics.

Author Contributions: Conceptualization, T.H. and F.Z.; methodology, T.H.; software, T.H.; validation, T.H.; formal analysis, T.H. and F.Z.; investigation, J.H.; resources, J.H.; data curation, T.H.; writing—original draft preparation, T.H.; writing—review and editing, M.K.; visualization:, T.H.; supervision, F.Z., J.H. and M.K.; project administration, F.Z., M.K. and J.H.; funding acquisition, J.H. All authors have read and agreed to the published version of the manuscript.

Funding: This research received no external funding.

Institutional Review Board Statement: This study did not require ethical approval.

Data Availability Statement: Data is contained within the article.

Acknowledgments: The authors acknowledge the support of the Bundeswehr Research Institute for Materials, Fuels, and Lubricants, whose laboratory equipment and 3D printers could be used for this work. The authors also acknowledge financial support by the University of the Bundeswehr Munich.

Conflicts of Interest: The authors declare no conflicts of interest.

References

1. Wiklund, J.; Karakoç, A.; Palko, T.; Yiğitler, H.; Ruttik, K.; Jäntti, R.; Paltakari, J. A Review on Printed Electronics: Fabrication Methods, Inks, Substrates, Applications and Environmental Impacts. *J. Manuf. Mater. Process.* **2021**, *5*, 89. [CrossRef]
2. J.A.M.E.S GmbH. AME Drone, 18.04.2024. Available online: https://j-ames.com/partners/partners/james-gmbh/ame-drone (accessed on 20 May 2024).
3. Persad, J.; Rocke, S. Multi-material 3D printed electronic assemblies: A review. *Results Eng.* **2022**, *16*, 100730. [CrossRef]
4. Lopez-Villegas, J.M.; Vidal, N.; Salas, A. Design, manufacture and characterization of compact filter assemblies for radiofrequency applications. *Addit. Manuf.* **2021**, *48*, 102410. [CrossRef]
5. Rao, C.H.; Avinash, K.; Varaprasad, B.K.S.V.L.; Goel, S. A Review on Printed Electronics with Digital 3D Printing: Fabrication Techniques, Materials, Challenges and Future Opportunities. *J. Electron. Mater.* **2022**, *51*, 2747–2765. [CrossRef]
6. Wu, W.; Fang, Q. Design and simulation of printed spiral coil used in wireless power transmission systems for implant medical devices. In Proceedings of the Annual International Conference of the IEEE Engineering in Medicine and Biology Society. IEEE Engineering in Medicine and Biology Society. Annual International Conference, Boston, MA, USA, 30 August–3 September 2011; pp. 4018–4021. [CrossRef]
7. Sertoglu, K. Hensoldt Successfully Tests Its New 3D Printed Kalaetron Attack Radar Jammer. 30 June 2022. Available online: https://3dprintingindustry.com/news/hensoldt-successfully-tests-its-new-3d-printed-kalaetron-attack-radar-jammer-211676/ (accessed on 22 May 2024).
8. Marasco, I.; Niro, G.; Lamanna, L.; Piro, L.; Guido, F.; Algieri, L.; Mastronardi, V.M.; Qualtieri, A.; Scarpa, E.; Desmaële, D.; et al. Compact and flexible meander antenna for Surface Acoustic Wave sensors. *Microelectron. Eng.* **2020**, *227*, 111322. [CrossRef]
9. Zhu, J.; Yang, Y.; Li, M.; Mcgloin, D.; Liao, S.; Nulman, J.; Yamada, M.; Iacopi, F. Additively Manufactured Millimeter-Wave Dual-Band Single-Polarization Shared Aperture Fresnel Zone Plate Metalens Antenna. *IEEE Trans. Antennas Propag.* **2021**, *69*, 6261–6272. [CrossRef]
10. Filler, M.; Reinhardt, B. Nanomodular Electronics: Microelectronics Made Anywhere, Anytime, by Anyone. 15 February 2023. Available online: https://spec.tech/library/nanomodular-electronics-roadmap/NMERoadmap.pdf (accessed on 15 May 2024).
11. Urasinska-Wojcik, B.; Chilton, N.; Todd, P.; Elsworthy, C.; Bates, M.; Roberts, G.; Gibbons, G.J. Integrated manufacture of polymer and conductive tracks for real-world applications. *Addit. Manuf.* **2019**, *29*, 100777. [CrossRef]
12. Hensoldt AG. Hensoldt and Nano Dimension Achieve Breakthrough in Electronics 3D Printing: New Multi-Layer PCB Boosts Electronics Rapid Prototyping. 19 May 2020. Available online: https://www.hensoldt.net/news/1857/hensoldt-and-nano-dimension-achieve-breakthrough-in-electronics-3d-printing (accessed on 10 June 2024).
13. IEEE Electronics Packaging Society. Heterogeneous Integration Roadmap 2021. November 2021. Available online: https://eps.ieee.org/images/files/HIR_2021/ch08_smcfinal.pdf (accessed on 11 June 2024).
14. Chua, C.K. *3D Printing and Additive Manufacturing of Electronics: Principles and Applications*; World Scientific Series in 3D printing; World Scientific: Singapore, 2021.
15. Panesar, A.; Ashcroft, I.; Brackett, D.; Wildman, R.; Hague, R. Design framework for multifunctional additive manufacturing: Coupled optimization strategy for structures with embedded functional systems. *Addit. Manuf.* **2017**, *16*, 98–106. [CrossRef]
16. Wasserfall, F.; Hendrich, N.; Ahlers, D.; Zhang, J. Topology-aware routing of 3D-printed circuits. *Addit. Manuf.* **2020**, *36*, 101523. [CrossRef]
17. Park, Y.G.; Yun, I.; Chung, W.G.; Park, W.; Lee, D.H.; Park, J.U. High-Resolution 3D Printing for Electronics. *Adv. Sci.* **2022**, *9*, e2104623. [CrossRef]
18. Bowa, M. 3D Printed Electronics. Master's Thesis, University of Tennessee, Knoxville, TN, USA, 2017. Available online: https://trace.tennessee.edu/utk_gradthes/4998 (accessed on 10 May 2024).
19. Tan, H.W.; Choong, Y.Y.C.; Kuo, C.N.; Low, H.Y.; Chua, C.K. 3D printed electronics: Processes, materials and future trends. *Prog. Mater. Sci.* **2022**, *127*, 100945. [CrossRef]
20. Bhatia, A.; Sehgal, A.K. Additive manufacturing materials, methods and applications: A review. *Mater. Today Proc.* **2023**, *81*, 1060–1067. [CrossRef]
21. Sturgess, C.; Tuck, C.J.; Ashcroft, I.A.; Wildman, R.D. 3D reactive inkjet printing of polydimethylsiloxane. *J. Mater. Chem. C* **2017**, *5*, 9733–9743. [CrossRef]
22. Cho, D.W.; Lee, J.S.; Jang, J.; Jung, J.W.; Park, J.H.; Pati, F. Inkjet-based 3D printing. *Organ Print.* **2015**, Pages 3-1 to 3-7, Version: 20151001. [CrossRef]
23. Elkaseer, A.; Chen, K.J.; Janhsen, J.C.; Refle, O.; Hagenmeyer, V.; Scholz, S.G. Material jetting for advanced applications: A state-of-the-art review, gaps and future directions. *Addit. Manuf.* **2022**, *60*, 103270. [CrossRef]
24. *DIN EN ISO/ASTM 52900*; Additive Manufacturing–General Principles–Fundamentals and Vocabulary. International Organization for Standardization: Geneva, Switzerland, March 2022.
25. Zapka, W. (Ed.) *Inkjet Printing in Industry*; Wiley: Hoboken, NJ, USA, 2022. [CrossRef]

26. Nano Dimension LTD. AME Materials Technical Datasheet. May 2023. Available online: https://www.nano-di.com/wp-content/uploads/2023/05/AME-Materials-Technical-Data-Sheet.pdf (accessed on 8 June 2024).
27. Aydemir, C.; Altay, B.N.; Akyol, M. Surface analysis of polymer films for wettability and ink adhesion. *Color Res. Appl.* **2021**, *46*, 489–499. [CrossRef]
28. Wang, P.; Li, J.; Wang, G.; He, L.; Yang, J.; Zhang, C.; Han, Z.; Yan, Y. Hybrid additive manufacturing based on vat photopolymerization and laser-activated selective metallization for three-dimensional conformal electronics. *Addit. Manuf.* **2023**, *63*, 103388. [CrossRef]
29. Jansson, E.; Lyytikäinen, J.; Tanninen, P.; Eiroma, K.; Leminen, V.; Immonen, K.; Hakola, L. Suitability of Paper-Based Substrates for Printed Electronics. *Materials* **2022**, *15*, 957. [CrossRef] [PubMed]
30. Elmore, W.C.; Heald, M.A. *Physics of Waves*, Unabridged ed.; Dover Publications: New York, NY, USA, 1985.
31. Henke, H. *Elektromagnetische Felder: Theorie und Anwendung*; Springer: Berlin, Germany, 2020.
32. Adamczyk, B. Skin Depth in Good Conductors. 31 January 2020. Available online: https://incompliancemag.com/article/skin-depth-in-good-conductors/ (accessed on 20 June 2024).
33. Yu, X.; Gong, X.; Podder, C.; Ludwig, B.; Chen, I.M.; Shou, W.; Alvidrez, A.; Chen, G.; Huang, X.; Pan, H. Additive Manufacturing of Sandwich–Structured Conductors for Applications in Flexible and Stretchable Electronics. *Adv. Eng. Mater.* **2021**, *23*. [CrossRef]
34. Dimension, N. DragonFly IV—Build, Test, and Iterate Electronics in a Single Day. 2023. Available online: https://www.nano-di.com/dragonfly-iv (accessed on 22 June 2024).
35. Cohen, Z. Additive Manufacturing with Nanoparticles for Electronics Development. 3 October 2019. Available online: https://www.nano-di.com/resources/blog/2019-additive-manufacturing-with-nanoparticles-for-electronics-development (accessed on 10 May 2024).
36. Nano Dimension LTD. 3D Printed Microelectronics & New Design Thinking: Applications Engineering. 5 October 2022. Available online: https://www.avt.et.tu-dresden.de/fileadmin/saet/Archiv_2011_2020/Treffen79/02_NANODIMENSION.pdf (accessed on 18 May 2024).
37. Fried, S. 3D Printing PCBs with Conductive Inks: Advantages and Disadvantages. 6 August 2019. Available online: https://www.nano-di.com/resources/blog/2019-3d-printing-pcbs-with-conductive-inks-advantages-and-disadvantages (accessed on 10 May 2024).
38. Ellingson; Steven, W. *Electromagnetics*; Open Textbook Library and Virginia Tech Publishing: Minneapolis, MN, USA; Blacksburg, VA, USA, 2020. [CrossRef]
39. Chen, L. *Microwave Electronics: Measurement and Materials Characterization*; Wiley: Chichester, UK, 2005.
40. El-Hawary, M. *Introduction to Electrical Power Systems*, 50th ed.; IEEE Press Series on Power Engineering; IEEE Press: Piscataway, NJ, USA, 2008.
41. von Hippel, A.R. (Ed.) *Dielectric Materials and Applications*; Artech House: London, UK, 1995.
42. Thue, W. *Electrical Power Cable Engineering*, 3rd ed.; Power engineering; CRC Press: Boca Raton, FL, USA, 2017.
43. Li, Y.; Diddens, C.; Segers, T.; Wijshoff, H.; Versluis, M.; Lohse, D. Evaporating droplets on oil-wetted surfaces: Suppression of the coffee-stain effect. *Proc. Natl. Acad. Sci. USA* **2020**, *117*, 16756–16763. [CrossRef] [PubMed]
44. Marin, A.; Karpitschka, S.; Noguera-Marín, D.; Cabrerizo-Vílchez, M.A.; Rossi, M.; Kähler, C.J.; Rodríguez Valverde, M.A. Solutal Marangoni flow as the cause of ring stains from drying salty colloidal drops. *Phys. Rev. Fluids* **2019**, *4*, 041601. [CrossRef]
45. Marin, A.; Karpitschka, S.; Noguera-Marín, D.; Cabrerizo-Vílchez, M.A.; Rossi, M.; Kähler, C.J.; Valverde, M.A.R. Solutal Marangoni flow as the cause of ring stains from drying salty colloidal drops. *arXiv* **2018**, arXiv:1809.07722. [CrossRef]
46. Ansys Electronics. *Ansys Q3D Extractor*; Ansys Electronics: Canonsburg, PA, USA, 2021.
47. Jones, M. Ansys High Frequency Structure Simulator (HFSS) Tutorial. 2017. Available online: https://indico.fnal.gov/event/13068/contributions/17083/attachments/11439/14607/MJones_-_HFSS_Tutorial_for_Axion_Cavity_Workshop.pdf (accessed on 15 May 2024).
48. Griffiths, D.J. *Introduction to Electrodynamics*; Cambridge University Press: Cambridge, UK, 2019. [CrossRef]
49. Purcell, E.M. *Electricity and Magnetism*, 3rd ed.; Cambridge Univiversity Press: Cambridge, UK, 2013.
50. Feynman, R.P.; Leighton, R.B.; Sands, M. *The Feynman Lectures on Physics*, New Millennium, ed.; Basic Books: New York, NY, USA, 2011.
51. Ansys Electronics Suite. HFSS Help; Ansys Electronics Suite: Canonsburg, PA, USA, 2022.
52. Ansys Electronics Suite. *Q3D Extractor Help*; Ansys Electronics Suite: Canonsburg, PA, USA, 2022.
53. Huray, P. *The Foundations of Signal Integrity*; Wiley: Hoboken, NJ, USA, 2009; ISBN 978-0-470-34360-9.

Disclaimer/Publisher's Note: The statements, opinions and data contained in all publications are solely those of the individual author(s) and contributor(s) and not of MDPI and/or the editor(s). MDPI and/or the editor(s) disclaim responsibility for any injury to people or property resulting from any ideas, methods, instructions or products referred to in the content.